Broadband Fourier-transform silicon nitride spectrometer with wide-area multiaperture input

David González-Andrade,[1,*] Thi Thuy Duong Dinh,[2] Sylvain Guerber,[2,3] Nathalie Vulliet,[3] Sébastien Cremer,[3] Stephane Monfray,[3] Eric Cassan,[2] Delphine Marris-Morini,[2] Frédéric Boeuf,[3] Pavel Cheben,[4,5] Laurent Vivien,[2] Aitor V. Velasco,[1] and Carlos Alonso-Ramos[2]

[1]*Instituto de Óptica Daza de Valdés, Consejo Superior de Investigaciones Científicas (CSIC), Madrid 28006, Spain*
[2]*Centre de Nanosciences et de Nanotechnologies, CNRS, Université Paris-Sud, Université Paris-Saclay, Palaiseau 91120, France*
[3]*STMicroelectronics SAS, 850 rue Jean Monnet, 38920 Crolles, France*
[4]*National Research Council Canada, 1200 Montreal Road, Bldg. M50, Ottawa, Ontario K1A 0R6, Canada*
[5]*Center for Research in Photonics, University of Ottawa, Ottawa, Ontario K1N 6N5, Canada*
**Corresponding author: david.gonzalez@csic.es*

Received XX Month XXXX; revised XX Month, XXXX; accepted XX Month XXXX; posted XX Month XXXX (Doc. ID XXXXX); published XX Month XXXX

Integrated microspectrometers implemented in silicon photonic chips have gathered a great interest for diverse applications such as biological analysis, environmental monitoring, and remote sensing. These applications often demand high spectral resolution, broad operational bandwidth, and large optical throughput. Spatial heterodyne Fourier-transform (SHFT) spectrometers have been proposed to overcome the limited optical throughput of dispersive and speckle-based on-chip spectrometers. However, state-of-the-art SHFT spectrometers in near-infrared achieve large optical throughput only within a narrow operational bandwidth. Here we demonstrate for the first time, to the best of our knowledge, a broadband silicon nitride SHFT spectrometer with the largest light collecting multiaperture input (320×410 μm²) ever implemented in an SHFT on-chip spectrometer. The device was fabricated using 248 nm deep-ultraviolet lithography, exhibiting over 13 dB of optical throughput improvement compared to a single-aperture device. The measured resolution varies between 29 pm and 49 pm within the 1260 – 1600 nm wavelength range.

http://dx.doi.org/10.1364/OL.99.099999

Optical spectroscopy has been extensively employed to study the interaction between light and matter, enabling the identification of specific molecules and compounds through emission, scattering, or absorption of light [1]. In particular, the near-infrared (near-IR) spectral range, covering the wavelengths between 800 nm and 2500 nm, has undergone a renaissance of interest with applications ranging from food industry, chemical and biological analysis, medical research to environmental monitoring [2,3]. Benchtop spectrometers provide high spectral resolution and broadband operation for multi-target detection, yet these spectroscopic systems rely on large-scale bulk optical instruments. Conversely, miniaturized spectrometers have emerged as a promising solution to perform *in situ* analysis with handheld devices, or remote sensing with microsatellites and unmanned vehicles [4].

The high refractive index material platforms and CMOS compatibility of silicon photonics has enabled the development of high-performance optical spectrometers in extremely compact and robust form factors. Numerous on-chip silicon photonic spectrometers have been proposed based on different operational principles. Light dispersion has been exploited in planar waveguide devices [5,6] including arrayed waveguide gratings, echelle gratings, microring resonators, photonic crystals, and digital planar holograms [7-11]. Although sub-nanometer spectral resolutions can be achieved with these devices, they suffer from limited optical throughput [12]. Note that the optical throughput is also referred to as *étendue*. More recently, spectrometers based on wavelength-dependent speckle patterns have been proposed exhibiting fine resolutions and operation over broad wavelength ranges [13-15]. Since the spectral-to-spatial mapping of this kind of spectrometers is generated and recorded after the device fabrication, the transmission matrix can be calibrated to mitigate the influence of chip fabrication errors. Nevertheless, speckle-based spectrometers are still hampered by a low sensitivity owing to their single input aperture and the high losses caused by scattering in disordered media, out-of-plane leakage, and evanescent coupling in long multimode waveguides. Fourier-transform (FT) spectrometers, on the other hand, provide a high resolution along with an improved optical throughout as they benefit from Jacquinot's advantage [12].

In this case, the input light spectrum is calculated using the discrete FT of the interferogram detected at the output. Depending on how this output interferogram is generated, state-of-the-art on-chip FT spectrometers can be divided into three main groups: i) active scanning, ii) stationary wave integrated, and iii) spatial heterodyne spectrometers. In active scanning FT spectrometers, the optical path difference is modified over time by changing either the physical path length [16] or the optical properties of the waveguides by means of the thermo-optic effect [17]. Unlike the scanning devices, stationary wave integrated FT (SWIFT) spectrometers and spatial heterodyne FT (SHFT) spectrometers do not involve any moving or active components. Reported SWIFT spectrometers operate over a broad bandwidth of ~100 nm but have only shown moderate spectral resolutions (4 nm [18], 6 nm [19]), whereas SHFT spectrometers based on an array of Mach-Zehnder interferometers (MZIs) can yield resolutions on the order of a few tens of picometers [20-22]. However, the operation bandwidth of state-of-the-art SHFT spectrometers in the near-IR wavelengths is limited by the strong modal dispersion of silicon-on-insulator and silicon nitride (SiN) waveguides, hindering multi-target detection with a single spectrometer [23]. On the other hand, mid-IR SHFT spectrometers have been demonstrated that exploit optimized waveguide geometry to achieve wide bandwidth and dual-polarization operation [24]. Still, there is no demonstration of on-chip SHFT spectrometers achieving wideband operation and large optical throughput simultaneously.

In this Letter, we design and experimentally demonstrate a broadband on-chip SHFT spectrometer for the SiN platform that operates at near-IR wavelengths for transverse-electric (TE) polarized light. Instead of employing several parallel spectrometers optimized for different spectral band operation as reported in [25], we use high-performance SiN beam splitters to implement the array of MZIs and thus overcome the inherent limitations posed by conventional power splitters in terms of losses, imbalance, and operating bandwidth. Furthermore, we have also optimized the light collection system at the input to cover a wide area and thereby improve the optical throughput.

One of the key advantages of SHFT spectrometers is the capability of implementing multiaperture input configurations. Our input surface grating coupler, depicted in Fig. 1, leverages this advantage by covering an extensive area of 320×410 μm² (W_{GC}×L_{GC}) and coupling light simultaneously to all 16 MZIs. The coupler is designed for TE polarization and both width and length were chosen to optimize the overlap between the fundamental mode of the pigtailed gradient-index (GRIN) fiber collimator (near-Gaussian distribution) and the radiated field (exponential distribution). The diffractive section of the input grating comprises unetched 600-nm-thick SiN segments of length $a = 630$ nm and shallow-etched segments of length $\Lambda - a = 395$ nm with an etch depth of 300 nm. The lower refractive index contrast of the SiN platform compared to SOI combined with the shallow-etched waveguide geometry results in a reduced grating contrast that weakens the grating radiation strength and correspondingly increases the grating length. This allows us to maximize the input aperture of the SHFT chip based on multiple smaller apertures. It should be noted that the optical throughput is the product of the solid angle and the input area [12,26]. Interconnection between the wide-area diffraction grating and the 700-nm-wide waveguides of the MZIs is implemented with 16 linear tapers with a length of $L_T = 500$ μm. The calculated coupling efficiency is -6.9 dB at the wavelength of 1563 nm with a 3-dB bandwidth of 18.2 nm. The full wavelength range between 1260 nm and 1600 nm wavelength is characterized by adjusting the tilt angle of the GRIN collimator and the SMF-28 fiber, addressing different portions of the spectrum.

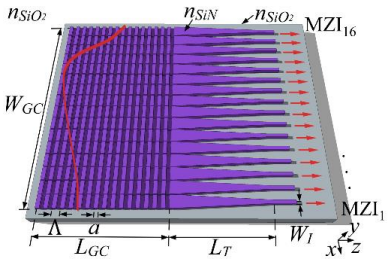

Fig. 1. 3D schematic of the wide-area input grating coupler, which consists of a 1D diffraction grating and 16 linear tapers. A Gaussian field with a 500 μm beam waist is coupled into the chip and simultaneously feeds the array of 16 MZIs (in red). Dimensions are not to scale.

MZIs comprise two identical 1×2 SiN beam splitters in back-to-back configuration with an increasing arm imbalance. The maximum path length difference between MZI arms is 22.8 mm and the minimum bend radius is 30 μm. The choice of the beam splitters is important as they ultimately determine the operating bandwidth of our spectrometer. The selected splitters exhibit low losses and low power imbalance (<0.6 dB) over a broad bandwidth of 420 nm (1260 – 1680 nm) [27]. The output port of each MZI is connected to a conventional grating coupler whose width and length are 13.5 μm and 66.7 μm, respectively. The period of these conventional grating couplers is $\Lambda = 1.14$ μm and the duty cycle (DC $= a/\Lambda$) is 50%.

The SHFT spectrometer was fabricated in the industrial-scale 300 mm silicon photonics R&D platform at STMicroelectronics [28]. A SiN layer with a thickness of 600 nm was deposited onto a 1.4-μm-thick SiO_2 layer using low-temperature plasma-enhanced chemical vapor deposition (PECVD). The SiN layer was then patterned using 248 nm deep-ultraviolet (deep-UV) lithography and etched through a dry etching process. Finally, a 1.5 μm SiO_2 cladding was deposited. Figure 2(a) shows an optical image of the fabricated SHFT spectrometer, which comprises a wide-area input grating coupler, an array of 16 MZIs with varying optical path difference, and 16 conventional output grating couplers (see Figs.

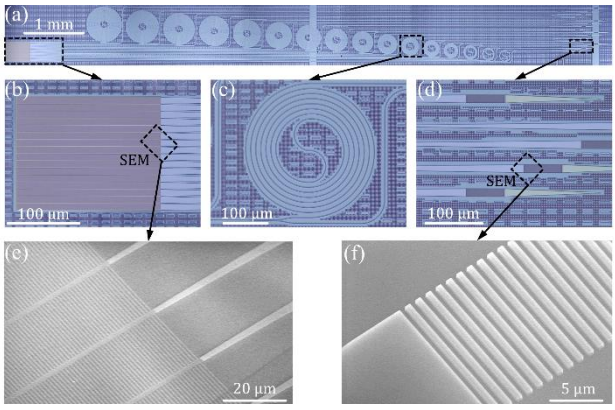

Fig. 2. Optical images of (a) the complete SHFT spectrometer, (b) the wide-area input grating coupler, (c) an MZI, and (d) output grating couplers. SEM images of the (e) input and (f) output grating couplers.

2(b), 2(c) and 2(d), respectively). Scanning electron microscope (SEM) images of the input and output grating couplers are also shown in Figs. 2(d) and 2(e), respectively. The entire device only occupies 9.8 × 0.9 mm^2.

Since dissimilar input and output fiber-chip coupling interfaces are implemented, input and output optical fibers are also different. A single-mode pigtailed GRIN fiber collimator is used at the input to couple a Gaussian field with a 500 μm beam waist into the chip via the wide-area grating coupler. Cleaved single-mode optical fiber (SMF-28) is employed for output coupling and subsequent light guiding to an external photodetector. Using this configuration, the enhancement in optical throughput is first evaluated with a tunable laser near 1563 nm. The GRIN fiber collimator at the input was aligned with the center of the wide-area grating coupler (maximizing the transmittance of MZI number 8). For the sake of comparison, auxiliary test structures consisting of two conventional grating couplers connected back-to-back were also measured using GRIN fiber collimator at the input and cleaved SMF-28 fiber at the output. Figure 3(a) shows the measured transmittance of each MZI normalized with respect to the transmission of the two conventional grating couplers in back-to-back configuration. This first assessment indicates that indeed the optical throughput improves compared to single-aperture auxiliary structures. In order to quantify the optical throughput improvement, the values of all MZI outputs are summed, resulting in a 13.1 dB optical throughput increase compared to conventional grating couplers. To verify the broadband operation of the SHFT spectrometer, three tunable lasers were used to cover the 1260 – 1600 nm wavelength range. Measurements in different spectral regions were carried out by adjusting the tilt angle of the GRIN collimator and the SMF-28 fiber independently. Waveguide insertion losses results in unequal fringe visibility along the interferometer array, causing a deviation from theoretical performance. The latter can be readily corrected

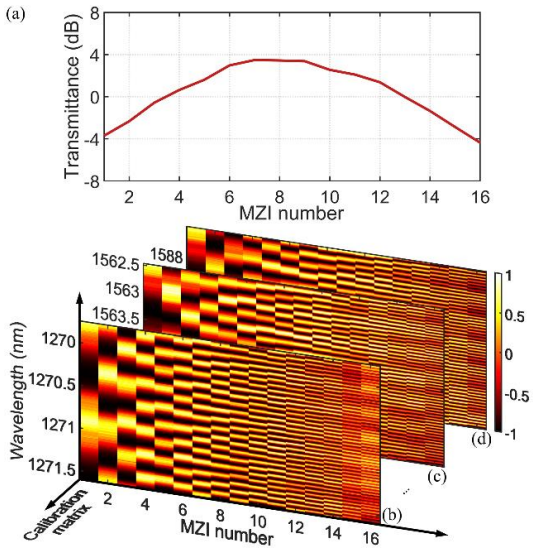

Fig. 3. (a) Measured transmittance of each MZI near 1563 nm normalized with respect to the transmission of two conventional grating couplers in back-to-back configuration. All measurements were carried out using a GRIN collimator at the input and an SMF-28 fiber at the output. 3D representation of the normalized calibration matrix measured for the 16 MZIs near (b) 1270, (c) 1563, and (d) 1588 nm.

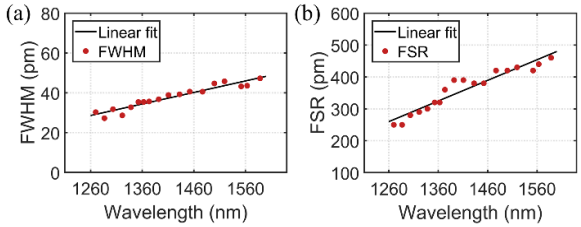

Fig. 4. (a) FWHM of the retrieved spectrum of a monochromatic input signal (red dots) and a linear fit (black line). (b) Free spectral range (FSR) of the SHFT spectrometer (red dots) and a linear fit (black line).

with the normalization of the output pattern by the visibility function of each MZI [20]. A total of 18 different calibration matrices were measured in different spectral regions within a bandwidth of 340 nm (1260 –1600 nm), being the tilt angle of the GRIN fiber collimator (input) and the SMF-28 optical fiber (output) different during the wavelength scan. Figures 3(b), 3(c), and 3(d) show the calibration matrices near the wavelengths of 1270, 1563 and 1588 nm, respectively. Power spectrum of the input signal is retrieved using a passive spectral retrieval algorithm based on the pseudoinverse of the calibration matrix [20,22]. The spatial interferogram measured at the output of each MZI at specific wavelengths $I(x_i, \lambda_j)$ is multiplied by the pseudoinverse of the corresponding calibration matrix $C_k^+(\lambda_j)$ in order to obtain the spectrum of the input signal $B(\lambda_j)$. This pseudoinverse retrieval algorithm can compensate amplitude and phase errors arising from fabrication deviations without the need for active control elements. Ripples in the retrieved spectrum arise from the truncation of the spatial interferogram in a specific wavelength range. To mitigate this effect, a Gaussian apodization window was used in our spectral retrieval algorithm. Figures 4(a) and 4(b) show the spectral resolution measured at full width at half maximum (FWHM) and the free spectral range (FSR) of the retrieved signals within the 1260 – 1600 nm wavelength range. The FSR in this device is defined as FSR $= \delta\lambda N/2$, where $\delta\lambda$ is the wavelength resolution and N is the number of MZIs in the array. Linear regression was applied to the experimental data set and is represented with a black line in both panels of Fig. 4. The spectral resolution is as low as 29 pm near 1260 nm wavelength and increases up to 49 pm at the wavelength of 1600 nm, while FSR values range from 260 nm to 470 nm within the same bandwidth. In Fig. 5, we show the experimentally retrieved spectrum of a monochromatic signal and a doublet of two monochromatic lines in six different spectral regions. Our SHFT spectrometer exhibits low sidelobe levels, yielding a high signal-to-noise ratio over the entire measured bandwidth. Complex spectral retrieval techniques such as those based on machine learning could also be employed to make our device more robust to varying environmental conditions [29].

In conclusion, we report on the demonstration of a broadband SHFT spectrometer implemented with 248 nm deep-UV lithography in a SiN platform. The limited operational bandwidth of conventional spectrometers in the near-IR region is circumvented with the inclusion of high-performance SiN beam splitter Furthermore, the chip input interface is designed to cover a large light collecting surface of 320×410 μm^2, leveraging the multiple surface grating couplers to exploit the Jacquinot's advantage. We estimated an improvement of the optical throughput of 13.1 dB compared with single-aperture device. The proposed spectrometer operates in a remarkable 340 nm bandwidth (1260 – 1600 nm),

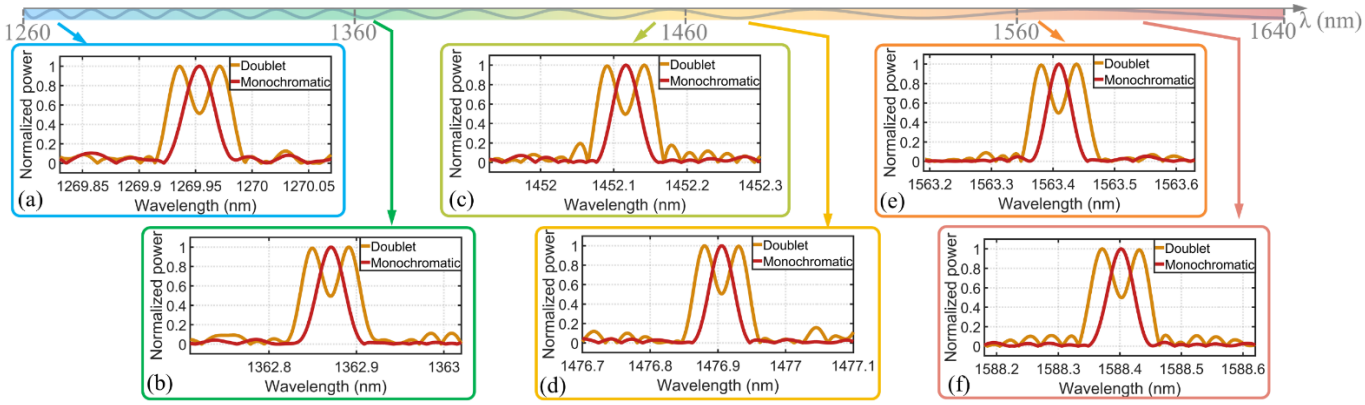

Fig. 5. Part of the near-infrared wavelength range and the retrieved spectrum of a monochromatic source (red curves) and a doublet of two monochromatic lines (orange curves) near the wavelengths of (a) 1270 nm, (b) 1363 nm, (c) 1452 nm, (d) 1477 nm, (e) 1563 nm, and (f) 1588 nm.

yielding a worst-case spectral resolution and FSR of 49 pm and 470 nm, respectively. Nevertheless, both resolution and free spectral range of our device could be further improved by using advanced retrieval methods, such as compressive-sensing reconstruction techniques, which have already been developed for SHFT spectrometers operating in the near-IR [30]. We believe that these results pave the way for the implementation of cost-effective on-chip spectrometers aimed at multi-target applications in the near-IR, such as environmental monitoring or chemical analysis.

Funding. Spanish Ministry of Science and Innovation (MICINN) (RTI2018-097957-B-C33, RED2018-102768-T, TEC2015-71127-C2-1-R FPI scholarship BES-2016-077798); Community of Madrid - FEDER funds (S2018/NMT-4326); Horizon 2020 Research and Innovation Program (Marie Sklodowska-Curie 734331); H2020 European Research Council (ERC POPSTAR 647342); European Commission (H2020-ICT-26127-2017 COSMICC 688516); French Industry Ministry (Nano2022 project under IPCEI program); Agence Nationale de la Recherche (ANR-MIRSPEC-17-CE09-0041).

Disclosures. The authors declare no conflicts of interest.

Data Availability. Data underlying the results presented in this paper are not publicly available at this time but may be obtained from the authors upon reasonable request.

References

1. C. Burgess, in *Encyclopedia of Analytical Science* (Elsevier, 2019), Vol. 8.
2. M. Ferrari and V. Quaresima, Neuroimage **63,** 921 (2012).
3. C. Pasquini, Anal. Chim. Acta **1026,** 8 (2018).
4. Z. Yang, T. Albrow-Owen, W. Cai, and T. Hasan, Science **371,** 6528 (2021).
5. P. Cheben, in *Optical Waveguides: From Theory to Applied Technologies* (CRC Press, 2007), pp. 173.
6. P. Cheben, A. Delâge, S. Janz, and D.-X. Xu, in *Advances in Information Optics and Photonics* (SPIE Press, 2008), pp. 599.
7. P. Cheben, J. H. Schmid, A. Delâge, A. Densmore, S. Janz, B. Lamontagne, J. Lapointe, E. Post, P. Waldron, and D.-X. Xu, Opt. Express **15,** 2299 (2007).
8. K. Ma, K. Chen, N. Zhu, L. Liu, and S. He, IEEE Photonics J. **11,** 4900107 (2019).
9. A. Nitkowski, L. Chen, and M. Lipson, Opt. Express **16,** 11930 (2008).
10. B. Momeni, E. S. Hosseini, M. Askari, M. Soltani, and A. Adibi, Opt. Commun. **282,** 3168 (2009).
11. G. Calafiore, A. Koshelev, S. Dhuey, A. Goltsov, P. Sasorov, S. Babin, V. Yankov, S. Cabrini, and C. Peroz, Light Sci. Appl. **3,** e203 (2014).
12. M. Florjańczyk, P. Cheben, S. Janz, A. Scott, B. Solheim, and D.-X. Xu, Opt. Express **15,** 18176 (2007).
13. B. Redding, S. F. Liew, R. Sarma and H. Cao, Nat. Photonics **7,** 746 (2013).
14. B. Redding, S. F. Liew, Y. Bromberg, R. Sarma, and H. Cao, Optica **3,** 956-962 (2016).
15. W. Hartmann, P. Varytis, H. Gehring, N. Walter, F. Beutel, K. Busch, and W. Perice, Adv. Opt. Mater. **8,** 1901602 (2020).
16. M. Erfan, Y. M. Sabry, M. Sakr, B. Mortada, M. Medhat, and D. Khalil, Appl. Spectrosc. **70,** 897 (2016).
17. M. C. M. M. Souza, A. Grieco, N. C. Frateschi, and Y. Fainman, Nat. Commun. **9,** 665 (2018).
18. E. Le Coarer, S. Blaize, P. Benech, I. Stefanon, A. Morand, G. Lérondel, G. Leblond, P. Kern, J. M. Fedeli, and P. Royer, Nat. Photonics **1,** 473 (2007).
19. X. Nie, E. Ryckeboer, G. Roelkens, and R. Baets, Opt. Express **25,** A409 (2017).
20. A. V. Velasco, P. Cheben, P. J. Bock, A. Delâge, J. H. Schmid, J. Lapointe, S. Janz, M. L. Calvo, D.-X. Xu, M. Florjańczyk, and M. Vachon, Opt. Lett. **38,** 706 (2013).
21. A. V. Velasco, P. Cheben, M. Florjańczyk, and M. L. Calvo, in *Progress in Optics* (Elsevier, 2014), Vol. 59, pp. 159.
22. A. Herrero-Bermello, A. V. Velasco, H. Podmore, P. Cheben, J. H. Schmid, S. Janz, M. L. Calvo, D.-X. Xu, A. Scott, and P. Corredera, Opt. Lett. **42,** 2239 (2017).
23. E. Ryckeboer, X. Nie, A. Dhakal, D. Martens, P. Bienstman, G. Roelkens, and R. Baets, in *IEEE 14th International Conference on Group IV Photonics (GFP)* (IEEE, 2017), p. 81.
24. Q. Liu, J. M. Ramirez, V. Vakarin, X. Le Roux, C. Alonso-Ramos, J. Frigerio, A. Ballabio, E. Talamas Simola, D. Bouville, L. Vivien, G. Isella, and D. Marris-Morini, Opt. Lett. **43,** 5021 (2018).
25. A. van Wijk, C. R. Doerr, Z. Ali, M. Karabiyik, and B. Imran Akca, Opt. Express **28,** 14618-14626 (2020).
26. T. T. D. Dinh, D. González-Andrade, M. Montesinos-Ballester, L. Deniel, B. Szelag, X. Le Roux, E. Cassan, D. Marris-Morini, L. Vivien, P. Cheben, A. V. Velasco, and C. Alonso-Ramos, Opt. Lett. **46,** 1341 (2021).
27. D. González-Andrade, S. Guerber, E. Durán-Valdeiglesias, D. Pérez-Galacho, X. Le Roux, N. Vulliet, S. Cremer, S. Monfray, E. Cassan, D. Marris-Morini, F. Boeuf, P. Cheben, L. Vivien, A. V. Velasco, and C. Alonso-Ramos, Opt. Lett. **45,** 527 (2020).
28. S. Guerber, C. Alonso-Ramos, D. Benedikovic, E. Durán-Valdeiglesias, X. Le Roux, N. Vulliet, E. Cassan, D. Marris-Morini, C. Baudot, F. Boeuf, and L. Vivien, IEEE Photonics Technol. Lett. **30**, 1679 (2018).
29. A. Herrero-Bermello, J. Li, M. Khazaei, Y. Grinberg, A. V. Velasco, M. Vachon, P. Cheben, L. Stankovic, V. Stankovic, D.-X. Xu, J. H. Schmid, and C. Alonso-Ramos, Opt. Lett. **44,** 5840 (2019).
30. H. Podmore, A. Scott, P. Cheben, A. V. Velasco, J. H. Schmid, M. Vachon, and R. Lee, Opt. Lett. **42,** 1440 (2017).